

Determination of the Zak phase of one-dimensional diffractive systems with inversion symmetry via radiation in Fourier space

C. Liu,^{*} H. R. Wang,^{*} and H. C. Ong[†]*Department of Physics, The Chinese University of Hong Kong, Shatin, Hong Kong, People's Republic of China*

(Received 9 January 2023; revised 8 June 2023; accepted 21 June 2023; published 5 July 2023)

Bloch waves in one-dimensional periodic systems carry the Zak phase, which plays a key role in determining the band topology. In general, for a system that possesses inversion symmetry, the Zak phase of an isolated band is quantized as 0 or π and is associated with the spatial-field symmetries of the Bloch waves at the Brillouin-zone center and boundary. Since the radiation losses from leaky systems are strongly associated with the Bloch waves, one may probe the far-field continuum to determine the Zak phases. Here, we formulate the radiations from photonic systems in Fourier space at the zone center and boundary and find they reveal the field symmetries and thereby the corresponding Zak phase. For verification, we have studied the Zak phases of TM plasmonic and TE photonic crystals by electrodynamic simulations and measuring the topological properties of plasmonic crystals using Fourier-space optical spectroscopy and common-path interferometry. In addition, a topologically protected interface state is demonstrated when two topologically trivial and nontrivial systems are joined together. Our results provide a simple way for characterizing the band topology of photonic systems via far fields.

DOI: [10.1103/PhysRevB.108.035403](https://doi.org/10.1103/PhysRevB.108.035403)

I. INTRODUCTION

Topological physics has attracted a widespread of interest not only in condensed-matter physics [1–3] but also in other branches such as ultracold atom [4,5], electromagnetism [6–8], mechanics [9], acoustics [10,11], and oceanography [12]. Much attention in this field focuses on realizing the so-called topologically protected states, which support robust wave propagation against perturbation and disorder [1–12]. When two topologically trivial and nontrivial systems are brought together, topological phase transition occurs at the interface between two systems to yield the Jackiw-Rebbi-type state [1–3]. As most of the matters are topologically trivial, the identification and the making of different classes of topological systems are currently under intensive investigation [13,14]. Likewise, developing methods to characterize the topological properties of the systems is also of great importance.

In analogy to the Su-Schrieffer-Heeger (SSH) model, the band topology of a one-dimensional (1D) periodic system is determined by Zak phase, γ , which is a geometric phase [15,16]. For the ℓ th isolated energy band, the γ_ℓ emerges when the Bloch wave travels adiabatically along the band across the first Brillouin zone from $k = -\pi/P$ to π/P , where P is the period of the system [16]. If the system possesses inversion symmetry, the γ_ℓ is quantized as either 0 or π [16]. The zero or π Zak phase defines the topological invariant of a two-band system. For a system that supports multiple bands, the topology of the band gap of interest is the summation of all γ_ℓ of the

bands below that gap, giving rise to the total γ that is either even or odd multiple of π for indicating whether the system is topologically trivial or nontrivial [17,18]. A zero-dimensional interface state is then formed between two odd and even π systems.

One notable feature that comes with γ is the distinctive spatial wave symmetries at the zone center and boundary of the band [16–18]. The field symmetries are the same for $\gamma = 0$ but different when $\gamma = \pi$ [18]. The association between γ and the field symmetry can be understood from the standpoint of the Wannier function, which sums the Bloch waves carrying all k along a band [19]. Considering the Bloch waves at two high-symmetry points that have the same field symmetry, the Wannier function has $W(-x) = \pm W(x)$ spatial dependence, leading to $\gamma = \frac{2\pi}{P} \int_{-\infty}^{\infty} x |W(x)|^2 dx = 0$ [16]. On the other hand, for the waves that exhibit different symmetries, the Wannier function now shows $W(-x + P) = \pm W(x)$ dependence, which gives $\gamma = \pi$ [16]. Remarkably, the quantization of γ and the associated field symmetries are carried over to non-Hermitian systems provided they still possess inversion symmetry [20]. Therefore, instead of tracing the Bloch waves one by one along the band to determine γ , one can simply examine the field symmetries. However, how to measure the spatial wave symmetry remains challenging.

To date, there are only a few studies focus on measuring the geometric phase, either Zak or Berry phase [21–24]. Demler and Bloch and their co-workers were among the first to combine Bloch oscillation and interferometry in a 1D dimerized cold-atom system to mobilize the Bloch wave across the Brillouin zone and subsequently measure the γ [21,22]. They prove, for an inversion symmetric system, $\gamma = \pi$ evolves when the intercell interaction is stronger than that of intracell. Cardano *et al.* have demonstrated the use of mean

*These authors contributed equally to this work.

†hcong@phy.cuhk.edu.hk

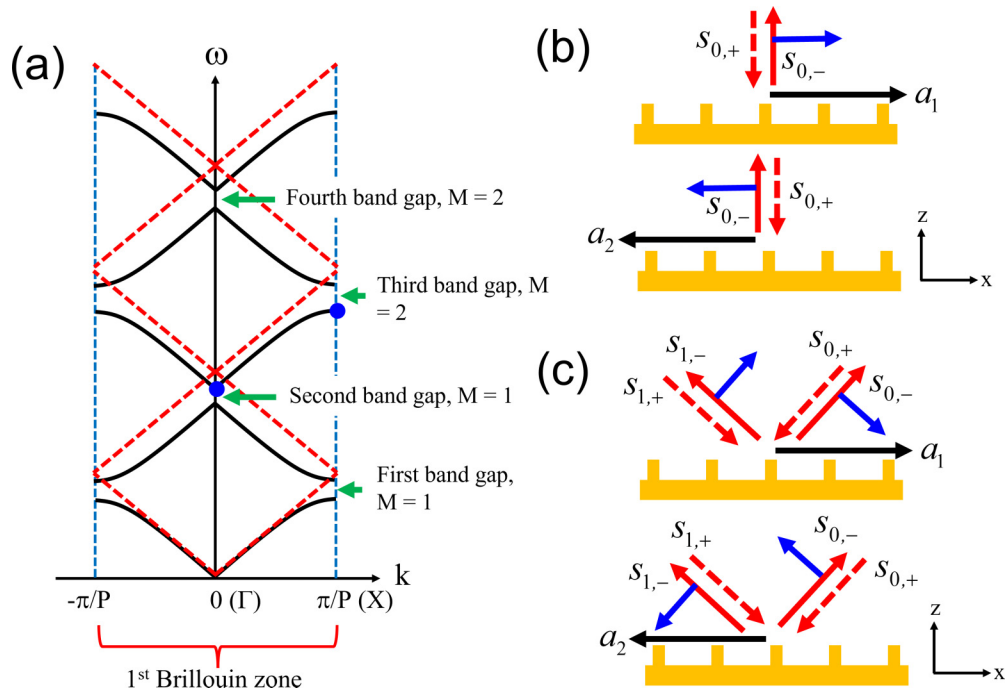


FIG. 1. (a) The ω - k plot of a 1D optical system that supports guided resonances. Solid and dashed lines are resonant Bloch modes and the Wood anomalies deduced by using the phase-matching equation. Bloch modes form continuous energy bands that are split by band gaps at Γ and X points in the first Brillouin zone. At the gap, two supermodes are formed at lower and higher energies. The Wood anomalies cross at the Γ and X points following $\lambda_o = P/M$ and $P/(M - 1/2)$. The supermodes of interest at the two points are marked by blue solid circles. (b) At the second gap, two Bloch-like modes $a_{1/2}$ propagate in opposite x directions, and each supports one $m = 0$ input and output ports $s_{0,\pm}$. Output radiation channels from $a_{1/2}$ carry linear polarizations pointing in opposite directions. (c) At the third gap, $a_{1/2}$ supports two mirror symmetric $m = 0$ and 1 input and output port $s_{0,\pm}$ and $s_{1,\pm}$ at $\pm\theta_i$. Polarizations of two output channels from a_1 point in same clockwise and counterclockwise directions to ensure continuity but are opposite to those from a_2 .

displacement method to determine γ in a chiral Floquet system [23]. Such method is then extended to other more-generalized SSH systems where the next-nearest neighbor interaction is strong enough to break the chiral symmetry [24]. While most of them focus on tracing the Bloch waves in momentum space, Gorlach *et al.* adopt an alternative approach by probing the spectral positions of the dipolar (bright) and quadrupolar (dark) supermodes at the zone center, which reveal the topological invariant of the system [25]. However, their method is limited to two-dimensional (2D) honeycomb systems that possess C_6 symmetry in which up and down pseudospins are found to define the nonzero spin Chern number [26]. Therefore, measuring the supermodes only at the zone center is sufficient to determine the band topology. In addition, it is applicable only to the lowest band gap above the light line but not the others at higher energy. Recently, Chan and co-workers formulated that the sign of the reflection phase for the wavelengths within the ℓ th band gap can resolve the γ_ℓ of 1D systems [17,18]. Although the approach has been applied to several photonic and acoustic systems, it is demonstrated specifically to stacked multilayer structures in which one single normal-reflection channel is supported for phase measurement [27–30]. Particularly, for photonic systems, a stringent interferometric configuration is required that may be difficult to be implemented to other more general systems such as corrugated surfaces [27].

Here, we have developed a simple approach to determine γ by measuring the radiations from photonic systems in Fourier

space at the Brillouin-zone center and boundary. It is shown that the radiation emitted by the supermodes exhibits a rich variety of characteristics such as quasibound state in the continuum (BIC) [31,32] and even- and odd mirror-symmetric diffraction pairs that reveal the near-field symmetry and the γ . To verify our formulation, we perform finite-difference time-domain (FDTD) simulations on 1D Au plasmonic and SiO_2/Au photonic crystals that, respectively, support TM- and TE-polarized guided waves. We then fabricate plasmonic crystals (PmCs) with different geometries and conduct polarization- and angle-resolved diffraction and phase spectroscopy by Fourier-space optical microscopy and common-path interferometry to study γ . Both the simulation and experimental results agree very well with the theory. Finally, a topologically protected interface state is demonstrated by joining two topologically trivial and nontrivial PmCs together.

II. TEMPORAL COUPLED-MODE THEORY

Assume a 1D optically thick periodic system that supports guided Bloch modes in the Γ - X direction is excited by light illuminated from the reflection side. Figure 1(a) illustrates the TM- or TE-polarized ω - k plot with the in-plane wave vector $k = 2\pi \sin\theta_i/\lambda$, where θ_i is the incident angle [33–36]. The plot is also known as dispersion relation, and it provides the necessary conditions for exciting the resonant modes in the system. In analogy to the band-folding scheme in electronic crystals [37], the excitation requires the

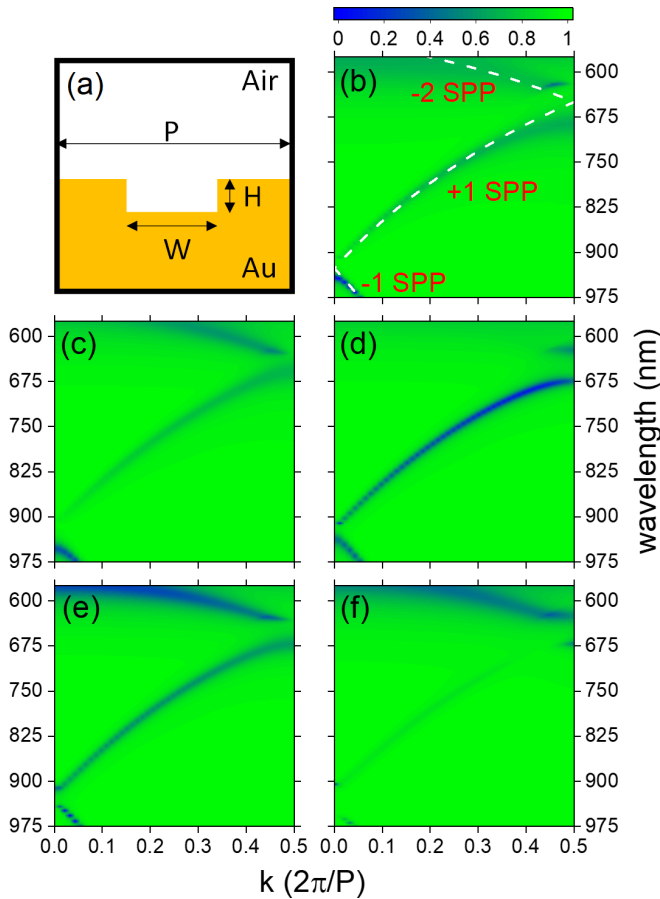


FIG. 2. (a) Unit cell of 1D PmC for FDTD simulations. Simulated TM-polarized k - and wavelength-resolved total reflectivity mappings of PmCs with W =(b) 100, (c) 250, (d) 400, (e) 550, and (f) 700 nm taken along Γ - X direction. white dashed lines are calculated by using phase-matching equation, indicating ± 1 and -2 Bloch-like SPPs are excited. At Γ and X points where $k = 0$ and 0.5 , two energy band gaps are formed, featuring two dark and bright modes located above or below gap. Particularly, at $k = 0$, a quasi-BIC is observed at either above or below gap.

incident light to fulfill the phase-matching equation given as $(k + n_B \frac{2\pi}{P})^2 = (n_{\text{eff}} \frac{\omega}{c})^2$, where n_B is the Bragg scattering order, c is the light speed, and P and n_{eff} are the period and the wavelength-dependent effective refractive index of the system, respectively [33,35,36]. Depending on n_B , the resonant modes form several continuous energy bands (solid lines) spanning across the first Brillouin zone and are divided by band gaps at the zone center (Γ) and boundary (X). The gap arises when two degenerate counterpropagating Bloch modes interact to yield two nonpropagating supermodes locating at higher and lower energies [33,34]. Because the n_{eff} of the system is larger than 1, the spectral positions of the supermodes are lower than the cross points of the Wood anomalies (WAs), where n_{eff} is taken to be 1 (dashed lines) [38]. The WA cross points at the Γ and X points are positioned at $\lambda_o = \frac{P}{M}$ and $\frac{P}{M-1/2}$, respectively, with M a natural number that increases sequentially with the cross-point position as shown in Fig. 1(a) [39]. In this study, we will focus on the band sandwiched between the second and third gaps with

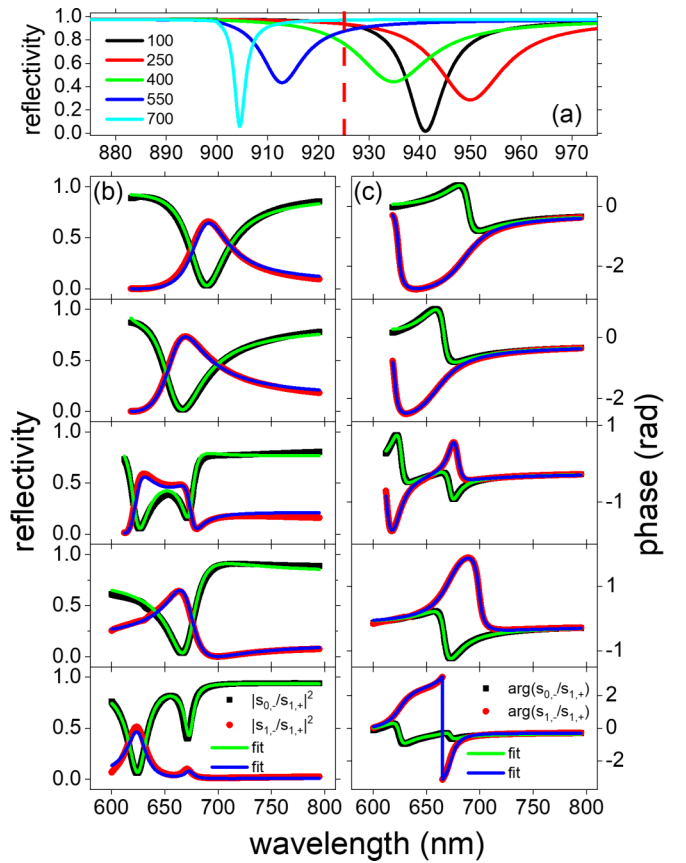


FIG. 3. TM-polarized total reflectivity spectra of PmCs taken at Γ point for different W , exhibiting only one single-reflectivity dip as bright mode. Red dashed line is band-gap center, indicating quasi-BIC occurs at shorter wavelength for $W = 100, 250$, and 400 nm but longer wavelength for $W = 550$ and 700 nm. At X point, two TM-polarized mirror-symmetric $m = 0$ (black square) and 1 (red circle) (b) reflectivity and (c) phase spectra for $W = 100$ (top) to 700 (bottom). Green and blue solid lines are best fits determined by CMT.

the supermodes of interest marked as two blue circles. The generalization to other higher-order bands will be provided in the Supplemental Material [39]. Given the system possesses inversion symmetry, the near-field symmetries of the supermodes sitting on the band thus define the γ .

As the system is leaky, once the supermode is excited, it will then dissipate into discrete radiation channels via diffraction. In fact, the output channels in Fourier space follow the grating equation given as $m\lambda = P(\sin\theta_i + \sin\theta_m)$, where θ_m is the diffraction angle with m the diffraction order [40]. For example, for the second band gap at the Γ point where $M = 1$ and $\lambda > \lambda_o = P$, the circled supermode supports only one single $m = 0$ specular diffraction order at $\theta_{m=0} = 0^\circ$, as shown in Fig. 1(b). Other nonzero m integers do not yield any propagating orders in the continuum. Likewise, for the third gap at $k = \pi/P$ in Fig. 1(c) where $M = 2$ and $\lambda > \lambda_o = 2P/3$, we see $\frac{2m-1}{3} \frac{\lambda}{\lambda_o} = \sin\theta_m$ results in $m = 0$ and 1 as the possible solutions, and $(2m-1)\sin\theta_i = \sin\theta_m$ shows two diffractions occur at $\theta_{m=0,1} = \pm\theta_i$. These two specular and back-reflected orders are mirror symmetric with respect to the surface normal of the system. Their sum will give the total reflection. In the

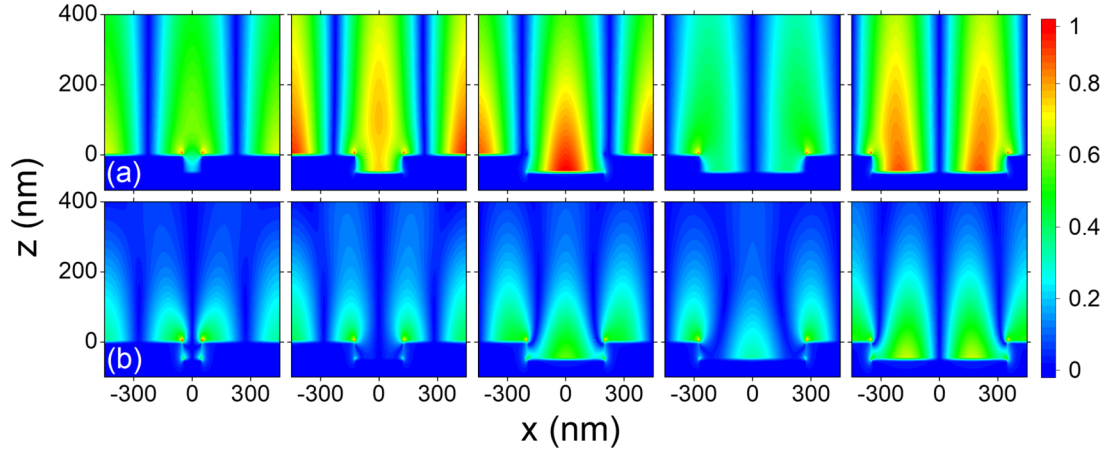


FIG. 4. FDTD-simulated $|E_z|$ near-field patterns of PmCs for different W taken at (a) Γ and (b) X points, showing their field symmetries are the same for $W=400$ and 550 nm but different for $W=100, 250$, and 700 nm.

Supplemental Material, we will extend the diffraction equation to higher band gaps and show that the number of channels from each supermode at the Γ and X points are $2(M-1)+1$ and $2(M-1)$ [39]. In addition, the $2(M-1)$ channels at two points are always presented as mirror-symmetric pairs. However, the normal diffraction order is present at the Γ point but is absent at the X point.

The interaction between two degenerate Bloch modes and the far-field channels can be formulated within the framework of temporal coupled mode theory (CMT) [41–44]. For a lossy and leaky system, at either the Γ or X point, the dynamics of two counterpropagating Bloch-mode amplitudes, a_1 and a_2 , taken under TM or TE polarization are written as

$$\frac{d}{dt} \begin{bmatrix} a_1 \\ a_2 \end{bmatrix} = i \begin{bmatrix} \tilde{\omega}_o & \tilde{\omega}_c \\ \tilde{\omega}_c & \tilde{\omega}_o \end{bmatrix} \begin{bmatrix} a_1 \\ a_2 \end{bmatrix} + K^T [s_{m,+}], \quad (1)$$

where $\tilde{\omega}_o$ and $\tilde{\omega}_c$ are the complex frequency and coupling constant, respectively, which are expressed as $\tilde{\omega}_o = \omega_o + i(\Gamma_a + \Gamma_r)/2$ and $\tilde{\omega}_c = \alpha + i\beta$, where ω_o is the resonant angular frequency, Γ_a and Γ_r are the absorption and radiative decay rates, and α and β are the real and imaginary parts of the coupling constant, respectively. The inhomogeneous part $K^T [s_{m,+}]$ defines the light from the continuum to drive a_1 and a_2 and their form depends on the number of available incident channels. For a given polarization, the reciprocal theorem requires that the discrete incoming power-amplitude vectors for the second and third gaps are $[s_{m,+}] = [s_{0,+}]$ and $[s_{1,+}]$, respectively, following the earlier grating equation, as illustrated in Figs. 1(b) and 1(c). The second and third gap K^T are given as $\begin{bmatrix} \tilde{\kappa}_{0,1} \\ \tilde{\kappa}_{0,2} \end{bmatrix}$ and $\begin{bmatrix} \tilde{\kappa}_{1,1} & \tilde{\kappa}_{1,2} \end{bmatrix}$, where the first and second subscripts of $\tilde{\kappa}_{m,n}$ are the diffraction order m and mode 1 or 2, and they define the complex in-coupling constant matrices.

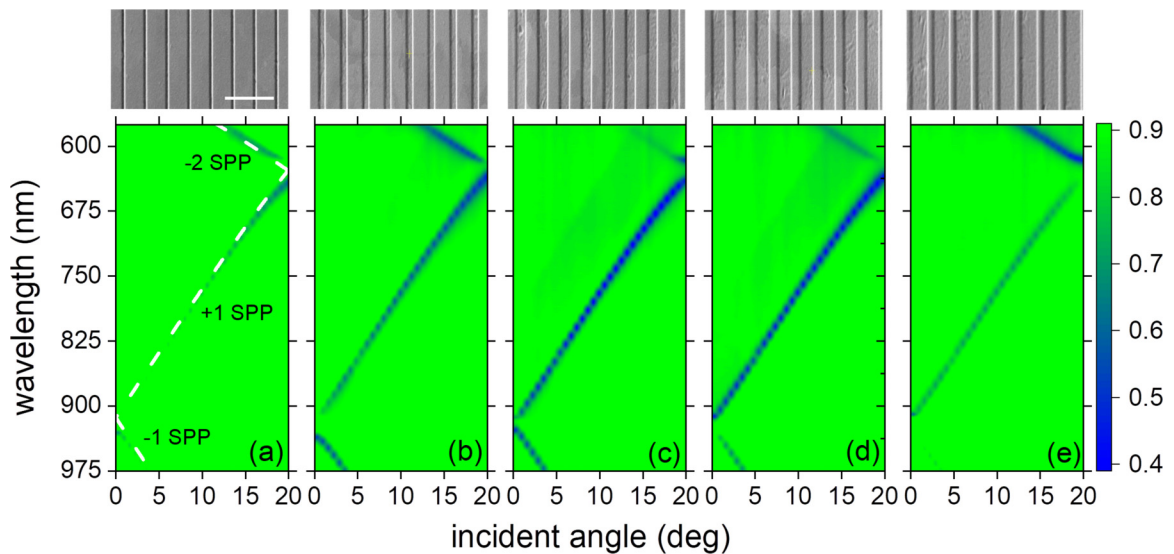


FIG. 5. Measured TM-polarized angle- and wavelength-resolved total reflectivity mappings of PmCs with $W=(a)$ 100, (b) 250, (c) 400, (d) 550, and (e) 700 nm taken along Γ - X direction. White dashed lines are ± 1 and -2 Bloch-like SPPs determined by the phase-matching equation. Two band gaps are formed at $\theta_i = 0^\circ$ and $\sim 20^\circ$, which correspond to Γ and X points. Insets are corresponding SEM images of PmCs with the scale bar = $2 \mu\text{m}$.

It is noted from Eq. (1) that if the system supports multiple input channels, light incident on only one of the channels is sufficient for excitation.

We will diagonalize Eq. (1) to provide a clearer physical picture. After solving the homogeneous part of Eq. (1), the complex frequencies of the supermodes are $\tilde{\omega}_{+/-} = \omega_{+/-} + i\Gamma_{+/-} = (\omega_o \pm \alpha) + i(\Gamma_a + \Gamma_r)/2 \pm \beta$, indicating their spectral positions and decay rates depend on α and β . We see the real part, $\omega_{+/-}$, of the supermodes are determined by the magnitude and sign of α and they are separated by a gap = 2α . On the other hand, for the imaginary part, $\Gamma_{+/-}$, one supermode has larger decay rate whereas another one has lower, featuring the bright and dark modes [45]. As the 2×2 matrix is non-Hermitian and symmetric, we then solve for the left eigenvectors to find the transformation matrix T to be $\sqrt{\frac{1}{2}} \begin{bmatrix} 1 & 1 \\ 1 & -1 \end{bmatrix}$, and it transforms $a_{1/2}$ to the supermodes as $\begin{bmatrix} a_+ \\ a_- \end{bmatrix} = \sqrt{\frac{1}{2}} \begin{bmatrix} a_1 + a_2 \\ a_1 - a_2 \end{bmatrix}$, which are orthogonal despite the nonhermiticity [43]. Equation (1) is then diagonalized as $\frac{d}{dt} \begin{bmatrix} a_+ \\ a_- \end{bmatrix} = i \begin{bmatrix} \tilde{\omega}_+ & 0 \\ 0 & \tilde{\omega}_- \end{bmatrix} \begin{bmatrix} a_+ \\ a_- \end{bmatrix} + TK^T [s_{m,+}]$, indicating $a_{+/-}$ are now driven individually without any interaction between them. The Fourier-space output channels can also be formulated properly. By using conservation of energy- and time-reversal symmetry, the outgoing radiation channels are expressed as $[s_{m,-}] = C[s_{m,+}] + K[a_2^{a_1}] = C[s_{m,+}] + KT[a_2^{a_+}]$, where C is the nonresonant scattering matrix [41,42]. Apparently, the radiation from $a_{+/-}$ is manifested by KT , which results from the superposition between the radiations from the uncoupled $a_{1/2}$. Therefore, $[s_{m,-}]$ can be rewritten as

$$s_{0,-} = \tilde{c}s_{0,+} + \sqrt{\frac{1}{2}}[\tilde{\kappa}_{0,1} + \tilde{\kappa}_{0,2}]a_+ + \sqrt{\frac{1}{2}}[\tilde{\kappa}_{0,1} - \tilde{\kappa}_{0,2}]a_- \quad (2)$$

and

$$\begin{aligned} \begin{bmatrix} s_{0,-} \\ s_{1,-} \end{bmatrix} &= \begin{bmatrix} \tilde{c}_1 & \tilde{c}_2 \\ \tilde{c}_2 & \tilde{c}_1 \end{bmatrix} \begin{bmatrix} s_{0,+} \\ s_{1,+} \end{bmatrix} + \sqrt{\frac{1}{2}} \begin{bmatrix} \tilde{\kappa}_{0,1} + \tilde{\kappa}_{0,2} \\ \tilde{\kappa}_{1,1} + \tilde{\kappa}_{1,2} \end{bmatrix} a_+ \\ &+ \sqrt{\frac{1}{2}} \begin{bmatrix} \tilde{\kappa}_{0,1} - \tilde{\kappa}_{0,2} \\ \tilde{\kappa}_{1,1} - \tilde{\kappa}_{1,2} \end{bmatrix} a_-, \end{aligned} \quad (3)$$

indicating each supermode has one single-output channel at the second gap, but two at the third gap.

As the system possesses inversion symmetry, $a_{+/-}$ should carry odd and even spatial-field symmetries with respect to the unit-cell center provided they are orthogonal to each other [20]. Such feature eases the determination of γ . Without knowing the exact field symmetries of $a_{+/-}$, we expect the γ of a continuous band is 0 if both the circled supermodes at the Γ and X points in Fig. 1(a) are either a_+ or a_- but is π if both a_+ and a_- are found. To determine whether a_+ or a_- is present, we further simplify Eqs. (2) and (3) based on the relationships between $\tilde{\kappa}_{m,n}$ of a mirror-symmetric diffraction pair. As an example, for the third gap in Fig. 1(c), the system symmetry requires $|\tilde{\kappa}_{0,1}| = |\tilde{\kappa}_{1,2}|$ and $|\tilde{\kappa}_{0,2}| = |\tilde{\kappa}_{1,1}|$ for $a_{1/2}$ propagating in the opposite directions. Given the polarizations of the radiations from $a_{1/2}$ scale with $\tilde{\kappa}_{m,n}$ and the pair from each mode should have the polarizations pointing either in the same clockwise or counterclockwise direction, as indicated in Fig. 1(c), to ensure continuity, the symmetry fur-

ther requires two pairs carry opposite polarization directions, or $\tilde{\kappa}_{0,1} = -\tilde{\kappa}_{1,2}$ and $\tilde{\kappa}_{0,2} = -\tilde{\kappa}_{1,1}$. In fact, as we see in the Supplemental Material, for any mirror-symmetric $m = p$ and q pair, $\tilde{\kappa}_{p,1} = -\tilde{\kappa}_{q,2}$ and $\tilde{\kappa}_{p,2} = -\tilde{\kappa}_{q,1}$ [39]. As a result, Eq. (3) can be simplified as

$$\begin{aligned} \begin{bmatrix} s_{0,-} \\ s_{1,-} \end{bmatrix} &= \begin{bmatrix} \tilde{c}_1 & \tilde{c}_2 \\ \tilde{c}_2 & \tilde{c}_1 \end{bmatrix} \begin{bmatrix} s_{0,+} \\ s_{1,+} \end{bmatrix} + \sqrt{\frac{1}{2}} \begin{bmatrix} \tilde{\kappa}_{0,1} - \tilde{\kappa}_{1,1} \\ -(\tilde{\kappa}_{0,1} - \tilde{\kappa}_{1,1}) \end{bmatrix} a_+ \\ &+ \sqrt{\frac{1}{2}} \begin{bmatrix} \tilde{\kappa}_{0,1} + \tilde{\kappa}_{1,1} \\ \tilde{\kappa}_{0,1} + \tilde{\kappa}_{1,1} \end{bmatrix} a_-. \end{aligned} \quad (4)$$

Likewise, by applying the same argument to the second gap such that $\tilde{\kappa}_{0,1} = -\tilde{\kappa}_{0,2}$, we rewrite Eq. (2) as

$$s_{0,-} = \tilde{c}s_{0,+} + \sqrt{2}\tilde{\kappa}_{0,1}a_-, \quad (5)$$

where a_+ is always presented as a quasi-BIC whereas a_- is a bright mode, making a_+ the symmetry-protected BIC regardless of what the values of $[\tilde{\kappa}_{0,1} \ \tilde{\kappa}_{0,2}]^T$ are [32]. On the other hand, while the supermodes at the third gap in Eq. (4) are bright and dark, their assignment is difficult and relies on the interplay between the sign and magnitude of $\tilde{\kappa}_{0,1}$ and $\tilde{\kappa}_{1,1}$, which are strongly system-geometry dependent. We see a_+ is the bright mode if $\tilde{\kappa}_{0,1}\tilde{\kappa}_{1,1} < 0$ but is dark when > 0 . Interestingly, a_+ (a_-) can also be quasi-BIC if $|\tilde{\kappa}_{0,1}| = |\tilde{\kappa}_{1,1}|$ ($|\tilde{\kappa}_{0,1}| = -|\tilde{\kappa}_{1,1}|$), but such condition can only be met for certain geometry, which requires careful tuning of the system parameters.

We then explicitly formulate the discrete far-field channels. By considering only one single incident channel such that $[s_{m,+}] = [s_{0,+}]$ and $[s_{1,+}] = 0$, the scattering coefficients of the supermodes can be formulated as

$$\frac{s_{0,-}}{s_{0,+}} = \tilde{c} + \frac{2\tilde{\kappa}_{0,1}^2}{i(\omega - \tilde{\omega}_-)} \quad (6)$$

for the second gap, and

$$\begin{aligned} \frac{s_{0,-}}{s_{1,+}} &= \tilde{c}_2 - \frac{1}{2} \frac{(\tilde{\kappa}_{0,1} - \tilde{\kappa}_{1,1})^2}{i(\omega - \tilde{\omega}_+)} + \frac{1}{2} \frac{(\tilde{\kappa}_{0,1} + \tilde{\kappa}_{1,1})^2}{i(\omega - \tilde{\omega}_-)}, \\ \frac{s_{1,-}}{s_{1,+}} &= \tilde{c}_1 + \frac{1}{2} \frac{(\tilde{\kappa}_{0,1} - \tilde{\kappa}_{1,1})^2}{i(\omega - \tilde{\omega}_+)} + \frac{1}{2} \frac{(\tilde{\kappa}_{0,1} + \tilde{\kappa}_{1,1})^2}{i(\omega - \tilde{\omega}_-)}, \end{aligned} \quad (7)$$

for the third gap. One sees the radiation losses from $a_{+/-}$ are Lorentzian, rendering Fano spectral profiles overall [46]. In addition, it is seen from Eq. (7) that the radiations of the mirror-symmetric pair from a_+ are π out of phase whereas those from a_- are in phase. Therefore, Eqs. (6) and (7) provide good tool for determining the spectral positions of $a_{+/-}$ by measuring the angle- and wavelength-resolved complex diffraction mapping of the system in Fourier space. While the position of the quasi-BIC, i.e., ω_+ , at the second gap can be visually identified from the mapping, the $\omega_{+/-}$ of the third gap are estimated by fitting the magnitude and phase, $|s_{0,-}/s_{1,+}|^2$ and $\arg(s_{0,-}/s_{1,+})$, spectra of the diffraction orders with Eq. (7) [39]. The extension of the CMT to any mirror-symmetric pair at higher-order band gap is provided in the Supplemental Material [39].

TABLE I. FDTD and experimental ω_{\pm} at Γ and X points for PmCs with different W . Highlighted are coupled modes located on +1 SPP band. If highlights at Γ and X points are both a_+ or a_- , Zak phase is 0. If not, Zak phase is π . Spectral positions of ω_+ at Γ point are visually approximated at nonzero k and incident angle.

		100 nm	250 nm	400 nm	550 nm	700 nm	
FDTD	Γ , zone center	ω_+ (eV)	~1.36	~1.37	~1.36	~1.32	~1.30
		ω_- (eV)	1.32	1.31	1.33	1.36	1.37
	X , zone boundary	ω_+ (eV)	2.12	2.03	1.84	1.85	1.98
		ω_- (eV)	1.81	1.88	1.99	1.97	1.84
	Zak phase		π	π	0	π	0
Experiment	Γ , zone center	ω_+ (eV)	~1.36	~1.36	~1.36	~1.33	~1.32
		ω_- (eV)	1.33	1.32	1.34	1.36	1.36
	X , zone boundary	ω_+ (eV)	2.02	2.01	1.94	1.95	2.01
		ω_- (eV)	1.94	1.96	2.01	2.00	1.95
	Zak phase		π	π	0	π	0

III. FINITE-DIFFERENCE TIME-DOMAIN SIMULATION

We verify the CMT model by FDTD simulations. Two types of optical systems are considered, and they are 1D Au plasmonic and SiO_2/Au photonic crystals. While the plasmonic crystals support TM-polarized Bloch-like surface plasmon polaritons (SPPs) [47], the photonic crystals (PhCs) excite TE waveguide modes [48]. We will present the results of PmCs here and those of the PhCs are provided in the Supplemental Material [39]. For the PmCs, the unit cell is shown in Fig. 2(a), with the period P and groove height H are set at 900 and 50 nm, respectively, and the groove width W is varied from 100 and 700 nm with a step size of 150 nm. The corresponding TM-polarized k - and λ -resolved total reflectivity mappings are calculated along the Γ - X direction in Figs. 2(b)–2(f), showing the dispersive Bloch-like SPP bands follow the phase-matching equation given as $\frac{\epsilon_{\text{Au}}}{\epsilon_{\text{Au}}+1}(\frac{1}{\lambda})^2 = (\frac{k}{2\pi} + \frac{n_B}{P})^2$, where ϵ_{Au} is the dielectric constant of Au, as illustrated by the dash lines in Fig. 2(b) for $n_B = \pm 1$ and -2 [33]. One sees the ± 1 SPP bands cross at the Γ point and $+1$ and -2 SPP bands intersect at the X point, forming two band gaps at $\lambda = 925$ and 650 nm and the supermodes. In agreement with the CMT model, the supermodes exhibit dark- (high-reflectivity) and bright- (low-reflectivity) radiation characteristics.

We will determine the Zak phase of the +1 SPP band, which is the band of interest in Fig. 1(a). At the Γ point for all PmCs, a quasi-BIC is always present, and it can be approximately visualized at the +1 band for $W = 100$ –400 nm but flips to the -1 band when W increases further by changing k slightly larger than zero. The corresponding reflectivity spectra are plotted in Fig. 3(a), clearly showing only one single-reflectivity dip is presented as the bright mode. As a result, we conclude a_+ locates at the +1 band for $W = 100$ –400 nm. On the other hand, at the X point, we no longer can differentiate the spectral positions of $a_{+/-}$ simply by examining the reflectivity spectra. We simulate the diffraction orders and find only the $m = 0$ and 1 mirror-symmetric orders exist in the continuum, following the grating equation well. The corresponding $|s_{0/1,-}/s_{1,+}|^2$ and $\arg(s_{0/1,-}/s_{1,+})$ spectra are calculated in Figs. 3(b) and 3(c) and fitted with Eq. (7) to determine the $\omega_{+/-}$, $\Gamma_{+/-}$, $\tilde{\kappa}_{0,1} - \tilde{\kappa}_{1,1}$, and $\tilde{\kappa}_{0,1} + \tilde{\kappa}_{1,1}$

of two supermodes by assuming both the $\tilde{c}_1(\lambda)$ and $\tilde{c}_2(\lambda)$ backgrounds complex constants [39,49,50]. The best fits are displayed as the solid lines. All the fitted $\omega_{+/-}$ of the PmCs are summarized in Table I, where the supermodes that sit on the +1 band are highlighted. Reminding if two highlights are either a_+ or a_- , the Zak phase is 0, but π when they are different [17,20]. We see in Table I $\gamma = \pi$ for $W = 100, 250,$ and 550 nm but $\gamma = 0$ for 400 and 700 nm.

To confirm our findings, we have simulated the $|E_z|$ near-field intensity profiles at the Γ and X points of the +1 band by FDTD in Figs. 4(a) and 4(b) for different W . At the Γ point, we see the $|E_z|$ profiles are even with respect to the groove center for $W = 100$ –400 nm but change to odd afterwards. On the other hand, the profiles at the X point are odd for $W = 100, 250,$ and 700 nm but are even for 400 and 550 nm. Despite the fact that the systems are non-Hermitian, the field symmetries of the supermodes are either odd or even [20]. As a result, the comparison between the field symmetries at the two points indicates $\gamma = \pi$ for $W = 100, 250,$ and 550 nm but 0 for 400 and 700 nm, inconsistent with the far-field determination.

IV. EXPERIMENTAL VERIFICATION

A series of 1D periodic Au rectangular groove PmCs has been fabricated by focused ion beam (FIB), and their scanning electron microscopy (SEM) images are shown in the insets of Fig. 5(a)–5(e), showing they have $P = 900$ nm, $H = 50$ nm, and W varying from 100 to 700 nm. After the sample preparation, the PmCs are then transferred to a homebuilt Fourier-space optical microscope described in the Supplemental Material for θ_i - and λ -resolved diffraction measurements [39]. Briefly, a supercontinuum generation laser is illuminated on the sample at a well-defined incident angle θ_i via the microscope objective lens, and the signals from the sample are collected by the same objective lens in which the diffraction orders are projected onto the Fourier space [51,52]. By using an aperture to filter out the desired diffraction order, a spectrometer-based charge-coupled device detector and a common-path interferometer are used for measuring the magnitude and phase spectra [53,54].

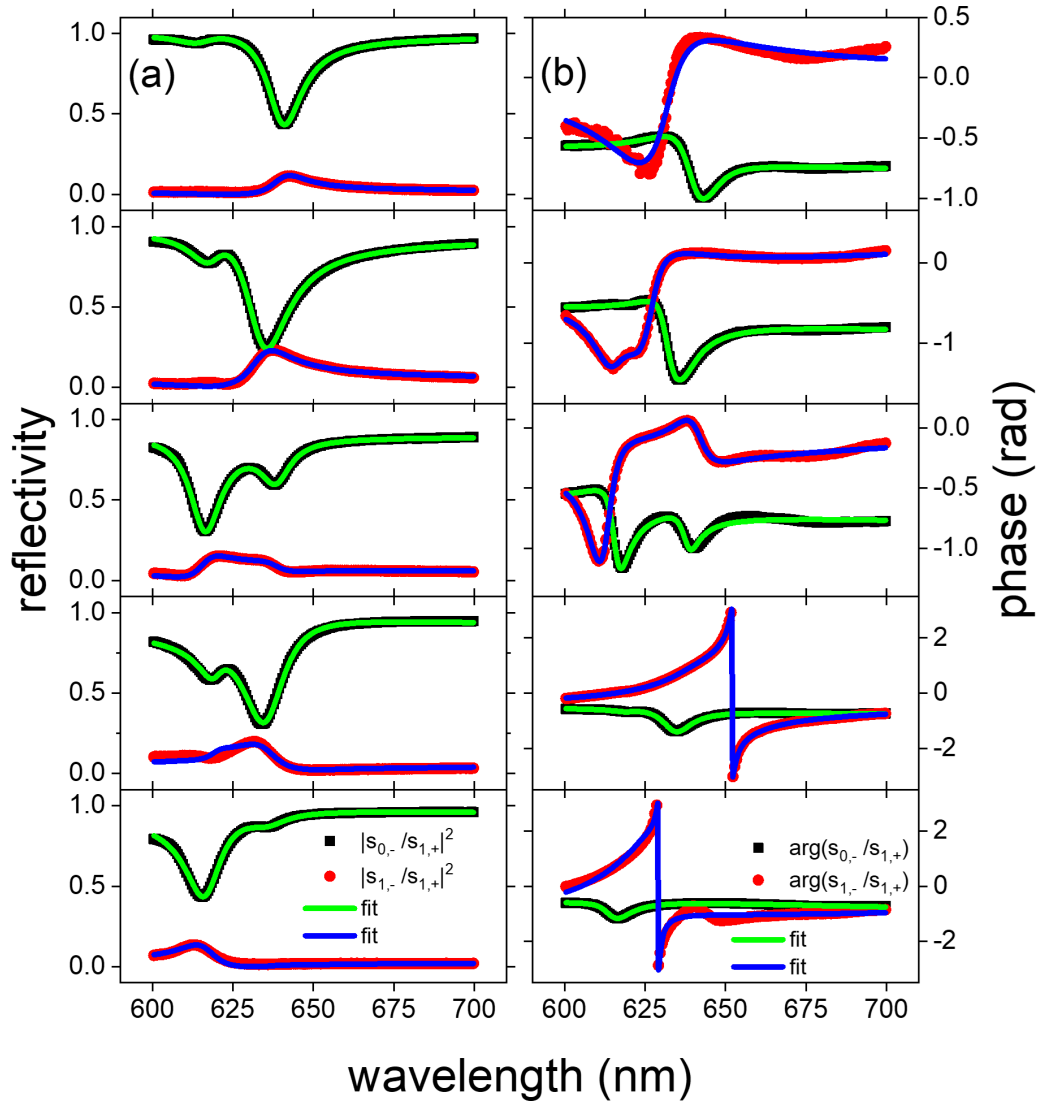


FIG. 6. At X point, two measured TM-polarized mirror-symmetric $m = 0$ (black square) and 1 (red circle) (a) reflectivity and (b) TM-TE phase-difference spectra for $W = 100$ (top) to 700 (bottom). Green and blue solid lines are best fits determined by CMT.

By varying θ_i sequentially and at the same time measuring the total reflection spectra, we contour plot the TM-polarized reflectivity mappings in Figs. 5(a)–5(e) for different W along the Γ - X direction. They show the $n_B = \pm 1$ and -2 SPP bands are present, and the bands are consistent with the phase-matching equation as illustrated by the dashed lines. From the mappings, we see at normal incidence, or the Γ point, BIC-like mode is always observed near the band gap and its position can be approximated visually at θ_i slightly larger than 0° . The $+1$ band has a_+ for $W = 100$ – 400 nm but a_- for larger W . On the other hand, at the X point where the $+1$ and -2 SPPs cross at $\theta_i \sim 20.5^\circ$, we see the dark and bright modes are found and their positions depend on W . To estimate the spectral positions of $a_{+/-}$, we measure the corresponding $m = 0$ and 1 diffraction and TM-TE phase-difference spectra in Figs. 6(a) and 6(b) and fit them by using Eq. (7) to determine the $\omega_{+/-}$ in Table I, which shows the $+1$ band is a_- for $W = 100, 250,$ and 700 nm, and is a_+ for 400 and 550 nm [39]. Therefore, $\gamma = \pi$ for $W = 100, 250,$ and 550 nm but $= 0$ for 400 and 700 nm in Table I.

Finally, we demonstrate a topologically protected state is formed at the interface between two topologically trivial and nontrivial PmCs [6,18]. We construct a heterostructure by joining two $W = 100$ - and 400 -nm PmCs together. Prior to joining, we have simulated by FDTD the field symmetries at the Γ and X points of two PmCs and determine the γ_ℓ of the $\ell = 0, -1,$ and $+1$ SPP bands to be $\pi, \pi,$ and π , respectively, for $W = 100$ nm, and $\pi, \pi,$ and 0 , respectively, for $W = 400$ nm. Therefore, the sums of γ_ℓ give 3π and 2π for $W = 100$ - and 400 -nm PmCs, indicating the $-2/+1$ (third) energy gaps at the X point are topologically nontrivial and trivial. We then simulate the heterostructure supercell as shown in Fig. 7(a) that consists of 14 unit cells of $W = 100$ - and 400 -nm PmCs on the right- and left-hand sides, respectively [55]. Figure 7(b) shows the TM-polarized k - and λ -resolved reflectivity mapping around the X point along the Γ - X direction, clearly demonstrating a localized mode is located at $k = 0.5$ or $\theta_i = 20.5^\circ$ and $\lambda \sim 640$ nm in the mid of the band gap formed by the crossing of $+1/-2$ SPPs. We also have simulated the λ -dependent near-field mapping of the

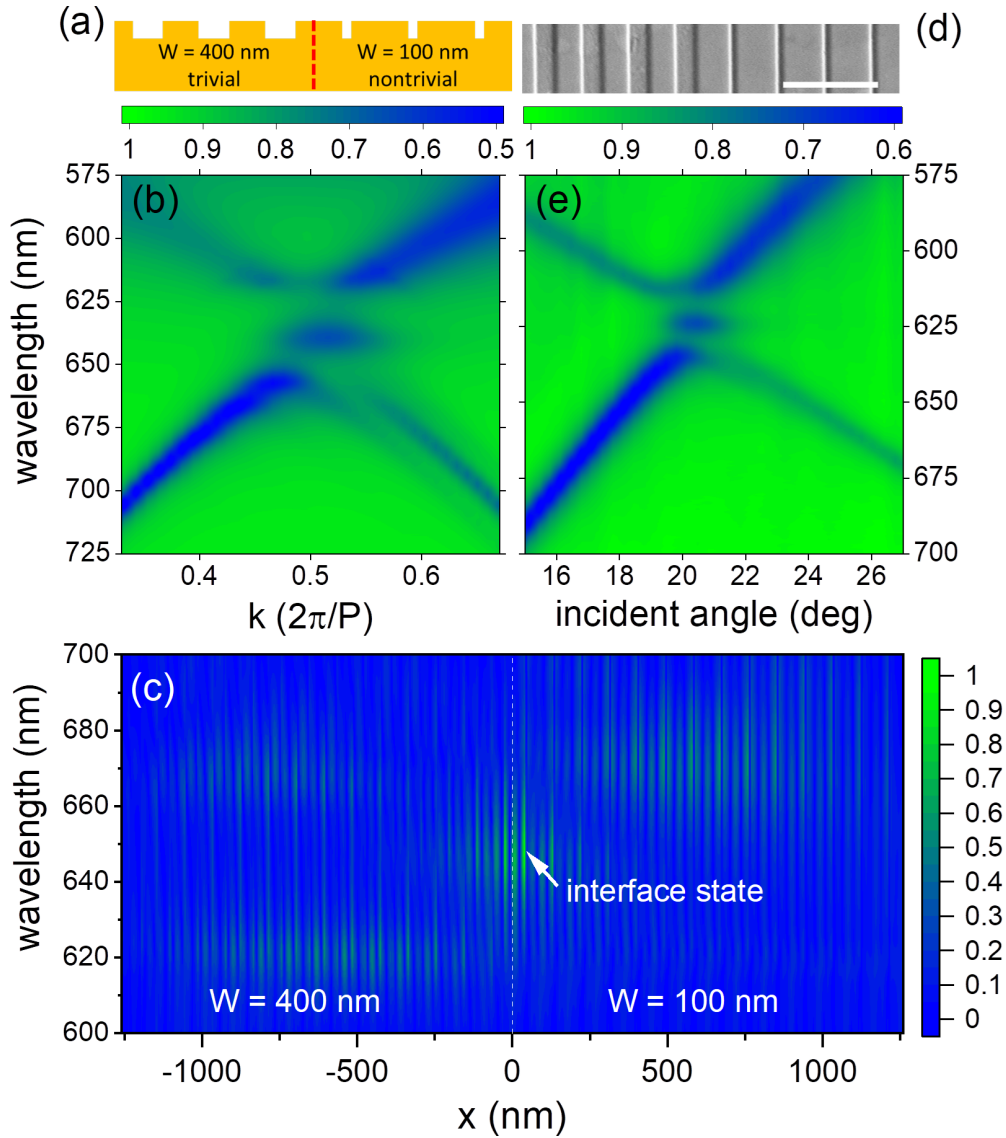


FIG. 7. (a) Schematic of heterostructure by joining $W =$ nontrivial 100- and trivial 400-nm PmCs. Interface is marked by the dashed line. (b) FDTD-simulated TM-polarized reflectivity mapping of heterostructure taken at X point along Γ - X direction, showing an interface state is found within gap at $\lambda = 640$ nm. (c) Wavelength-dependent near-field intensity mapping simulated at 20 nm above heterostructure. Interface is located at $x = 0$ μm , showing strong-field localization. Strong fields at 620 and 670 nm arise from the PmC bulk regions away from the interface due to the excitations of the upper and lower coupled modes. However, the strongest field strength is observed at the interface, $x = 0$ μm , at 640 nm, and it decays rapidly into the bulk regions, signifying the presence of a topologically protected interface state [55]. We have prepared the heterostructure by FIB and its SEM image is shown in Fig. 7(d) with $W =$ 100- and 400-nm PmCs on the right- and left-hand sides. The TM-polarized k - and wavelength-resolved reflectivity mapping of the sample is

illustrated in Fig. 7(e), showing a localized state is found at $\theta_i = 20.5^\circ$ and $\lambda \sim 625$ nm at the X point. We expect it to be an interface state as projected from the FDTD simulation.

heterostructure. For different λ , the near-field intensities at 20 nm above the surface is calculated across the heterostructure and then contour plotted in Fig. 7(c), showing the interface is located at $x = 0$ μm and the trivial and nontrivial regions are at $x > 0$ and < 0 μm , respectively. One sees two strong fields are visible at ~ 620 and 670 nm in the PmC bulk regions away from the interface due to the excitations of the upper and lower coupled modes. However, the strongest field strength is observed at the interface, $x = 0$ μm , at 640 nm, and it decays rapidly into the bulk regions, signifying the presence of a topologically protected interface state [55]. We have prepared the heterostructure by FIB and its SEM image is shown in Fig. 7(d) with $W =$ 100- and 400-nm PmCs on the right- and left-hand sides. The TM-polarized k - and wavelength-resolved reflectivity mapping of the sample is

V. CONCLUSION

In summary, we have developed a temporal CMT model to determine the Zak phase of an isolated band in 1D leaky photonic systems. At the Brillouin-zone center and boundary, we find the radiation losses from the supermodes in Fourier space present different characteristics ranging from quasi-BIC to odd or even mirror-symmetric diffraction pair, which are strongly associated with the spatial-field symmetries and thereby the corresponding Zak phase. For verification, 1D PmCs and PhCs that support TM- and TE-polarized SPP

and waveguide modes have been studied by FDTD and the results agree very well with the theory. We also have prepared 1D PmCs by FIB and examined their diffractions by using Fourier-space diffraction spectroscopy and common-path interferometry for determining the Zak phases. In the end, a topological protected interface state is demonstrated by joining two topologically trivial and nontrivial PmCs together.

ACKNOWLEDGMENTS

This research was supported by the Chinese University of Hong Kong through Area of Excellence (Grant No. AoE/P-02/12) and Innovative Technology Fund Guangdong-Hong Kong Technology Cooperation Funding Scheme (Grant No. GHP/077/20GD) and Partnership Research Program (Grant No. PRP/048/22FX).

-
- [1] X. L. Qi and S. C. Zhang, Topological insulators and superconductors, *Rev. Mod. Phys.* **83**, 1057 (2011).
- [2] M. Z. Hasan and C. L. Kane, Topological insulators, *Rev. Mod. Phys.* **82**, 3045 (2010).
- [3] J. E. Moore, The birth of topological insulators, *Nature (London)* **464**, 194 (2010).
- [4] N. R. Cooper, J. Dalibard, and I. B. Spielman, Topological bands for ultracold atoms, *Rev. Mod. Phys.* **91**, 015005 (2019).
- [5] D. W. Zhang, Y. Q. Zhu, Y. X. Zhao, H. Yan, and S. L. Zhu, Topological quantum matter with cold atoms, *Adv. Phys.* **67**, 253 (2019).
- [6] T. Ozawa, H. M. Price, A. Amo, N. Goldman, M. Hafezi, L. Lu, M. C. Rechtsman, D. Schuster, J. Simon, O. Zilberberg, and I. Carusotto, Topological photonics, *Rev. Mod. Phys.* **91**, 015006 (2019).
- [7] L. Lu, J. D. Joannopoulos, and M. Soljačić, Topological photonics, *Nat. Photonics* **8**, 821 (2018).
- [8] A. B. Khanikaev and G. Shvets, Two-dimensional topological photonics, *Nat. Photonics* **11**, 763 (2017).
- [9] S. D. Huber, Topological mechanics, *Nat. Phys.* **12**, 621 (2016).
- [10] Z. Yang, F. Gao, X. Shi, X. Lin, Z. Gao, Y. D. Chong, and B. Zhang, Topological Acoustics, *Phys. Rev. Lett.* **114**, 114301 (2015).
- [11] G. Ma, M. Xiao, and C. T. Chan, Topological phases in acoustic and mechanical systems, *Nat. Rev. Phys.* **1**, 281 (2019).
- [12] P. Delplace, J. B. Marston, and A. Venaille, Topological origin of equatorial waves, *Science* **358**, 1075 (2017).
- [13] F. Tang, H. C. Po, A. Vishwanath, and X. Wan, Comprehensive search for topological materials using symmetry indicators, *Nature (London)* **566**, 486 (2019).
- [14] X. Chen, X. Ma, K. He, J. F. Jia, and Q.-K. Xue, Molecular beam epitaxial growth of topological insulators, *Adv. Mater.* **23**, 1162 (2011).
- [15] W. P. Su, J. R. Schrieffer, and A. J. Heeger, Solitons in Polyacetylene, *Phys. Rev. Lett.* **42**, 1698 (1979).
- [16] J. Zak, Berry's Phase for Energy Bands in Solids, *Phys. Rev. Lett.* **62**, 2747 (1989).
- [17] M. Xiao, Z. Q. Zhang, and C. T. Chan, Surface Impedance and Bulk Band Geometric Phases in One-Dimensional Systems, *Phys. Rev. X* **4**, 021017 (2014).
- [18] M. Xiao, G. Ma, Z. Yang, P. Sheng, Z. Q. Zhang, and C. T. Chan, Geometric phase and band inversion in periodic acoustic systems, *Nat. Phys.* **11**, 240 (2015).
- [19] J. K. Asbóth, L. Oroszlány, and A. Pályi, *A Short Course on Topological Insulators* (Springer, New York, 2016).
- [20] S. R. Poccok, X. Xiao, P. A. Huidobro, and V. Giannini, Topological plasmonic chain with retardation and radiative effects, *ACS Photonics* **5**, 2271 (2018).
- [21] D. A. Abanin, T. Kitagawa, I. Bloch, and E. Demler, Interferometric Approach to Measuring Band Topology in 2D Optical Lattices, *Phys. Rev. Lett.* **110**, 165304 (2013).
- [22] M. Atala, M. Aidelsburger, J. T. Barreiro, D. Abanin, T. Kitagawa, E. Demler, and I. Bloch, Direct measurement of the Zak phase in topological Bloch bands, *Nat. Phys.* **9**, 795 (2013).
- [23] F. Cardano, A. D'Errico, A. Dauphin, M. Maffei, B. Piccirillo, C. de Lisio, G. De Filippis, V. Cataudella, E. Santamato, L. Marrucci, M. Lewenstein, and P. Massignan, Detection of Zak phases and topological invariants in a chiral quantum walk of twisted photons, *Nat. Commun.* **8**, 15516 (2017).
- [24] Z. Jiao, S. Longhi, X. Wang, J. Gao, W. Zhou, Y. Wang, Y. Fu, L. Wang, R. Ren, L.-F. Qiao, and X.-M. Jin, Experimentally Detecting Quantized Zak Phases without Chiral Symmetry in Photonic Lattices, *Phys. Rev. Lett.* **127**, 147401 (2021).
- [25] M. A. Gorbach, X. Ni, D. A. Smirnova, D. Korobkin, D. Zhirihin, A. P. Slobozhanyuk, P. A. Belov, A. Alù, and A. B. Khanikaev, Far-field probing of leaky topological states in all dielectric metasurfaces, *Nat. Commun.* **9**, 909 (2018).
- [26] L. H. Wu and X. Hu, Scheme for Achieving a Topological Photonic Crystal by Using Dielectric Material, *Phys. Rev. Lett.* **114**, 223901 (2015).
- [27] W. Gao, M. Xiao, C. T. Chan, and W. Y. Tam, Determination of Zak phase by reflection phase in 1D photonic crystals, *Opt. Lett.* **40**, 5259 (2015).
- [28] Q. Wang, M. Xiao, H. Liu, S. Zhu, and C. T. Chan, Measurement of the Zak phase of photonic bands through the interface states of a metasurface/photonic crystal, *Phys. Rev. B* **93**, 041415(R) (2016).
- [29] L. Fan, W. Yu, S. Zhang, H. Zhang, and J. Ding, Zak phases and band properties in acoustic metamaterials with negative modulus or negative density, *Phys. Rev. B* **94**, 174307 (2016).
- [30] W. Zhu, Y. Ding, J. Ren, Y. Sun, Y. Li, H. Jiang, and H. Chen, Zak phase and band inversion in dimerized one-dimensional locally resonant metamaterials, *Phys. Rev. B* **97**, 195307 (2018).
- [31] K. Koshelev, A. Bogdanov, and Y. Kivshar, Engineering with bound states in the continuum, *Opt. Photonics News* **31**, 38 (2020).
- [32] C. W. Hsu, B. Zhen, A. D. Stone, J. D. Joannopoulos, and M. Soljačić, Bound states in the continuum, *Nat. Rev. Mater.* **1**, 16048 (2016).
- [33] Z. L. Cao and H. C. Ong, Determination of the absorption and radiative decay rates of dark and bright plasmonic modes, *Opt. Exp.* **22**, 16112 (2014).
- [34] C. Billaudeau, S. Collin, C. Sauvan, N. Bardou, F. Pardo, and J.-L. Pelouard, Angle-resolved transmission measurements through anisotropic two-dimensional plasmonic crystals, *Opt. Lett.* **33**, 165 (2008).

- [35] N. Ganesh, W. Zhang, P. C. Mathias, E. Chow, J. A. N. T. Soares, V. Malyarchuk, A. D. Smith, and B. T. Cunningham, Enhanced fluorescence emission from quantum dots on a photonic crystal surface, *Nat. Nanotechnol.* **2**, 515 (2007).
- [36] A. Cerjan, C. Jörg, S. Vaidya, S. Augustine, W. A. Benalcazar, C. W. Hsu, G. Freymann, and M. C. Rechtsman, Observation of bound states in the continuum embedded in symmetry bandgaps, *Sci. Adv.* **7**, eabk1117 (2021).
- [37] C. Kittel, *Introduction to Solid State Physics* (Wiley, New York, 2004).
- [38] D. Maystre, Theory of Wood's Anomalies, in *Plasmonics: From Basics to Advanced Topics*, edited by S. Enoch and N. Bonod (Springer, New York, 2012), pp. 39.
- [39] See Supplemental Material at <http://link.aps.org/supplemental/10.1103/PhysRevB.108.035403> for the derivation of the number of radiation output channels of supermodes by grating equation, the generalization of the radiation channels of the supermode at the Brillouin-zone center and boundary, the fitting of the magnitude and phase spectra, the FDTD simulation results of 1D SiO₂/Au photonic crystals, and the Fourier-space optical microscope for angle- and wavelength-resolved diffraction mapping and common-path interferometry.
- [40] E. G. Loewen and E. Popov, *Diffraction Gratings and Applications* (CRC Press, New York, 1997).
- [41] H. A. Haus, *Waves and Fields in Optoelectronics* (Prentice-Hall, Englewood Cliffs, NJ, 1984).
- [42] S. Fan, in *Optical Fiber Telecommunications V Vol A: Components and Subsystems*, edited by I. Kaminow, T. Li, and A. E. Willner (Academic Press, Burlington, MA, 2008).
- [43] Z. L. Cao and H. C. Ong, Determination of complex Hermitian and anti-Hermitian interaction constants from a coupled photonic system via coherent control, *Opt. Exp.* **25**, 30611 (2017).
- [44] L. Verslegers, Z. Yu, Z. Ruan, P. B. Catrysse, and S. H. Fan, From Electromagnetically Induced Transparency to Superscattering with a Single Structure: A Coupled-Mode Theory for Doubly Resonant Structures, *Phys. Rev. Lett.* **108**, 083902 (2012).
- [45] C. Ropers, D. J. Park, G. Stibenz, G. Steinmeyer, J. Kim, D. S. Kim, and C. Lienau, Femtosecond Light Transmission and Subradiant Damping in Plasmonic Crystals, *Phys. Rev. Lett.* **94**, 113901 (2005).
- [46] M. F. Limonov, M. V. Rybin, A. N. Poddubny, and Y. S. Kivshar, Fano resonances in photonics, *Nat. Photonics* **11**, 543 (2017).
- [47] X. Guo, C. Liu, and H. C. Ong, Generalization of the Circular Dichroism from Metallic Arrays that Support Bloch-like Surface Plasmon Polaritons, *Phys. Rev. Appl.* **15**, 024048 (2021).
- [48] A. Christ, S. G. Tikhodeev, N. A. Gippius, J. Kuhl, and H. Giessen, Waveguide-plasmon Polaritons: Strong Coupling of Photonic and Electronic Resonances in a Metallic Photonic Crystal Slab, *Phys. Rev. Lett.* **91**, 183901 (2003).
- [49] C. M. B. Cordeiro, L. Cescato, A. A. Freschi, and L. Li, Measurement of phase differences between the diffracted orders of deep relief gratings, *Opt. Lett.* **28**, 683 (2003).
- [50] N. Destouches, H. Giovannini, and M. Lequime, Interferometric measurement of the phase of diffracted waves near the plasmon resonances of metallic gratings, *Appl. Opt.* **40**, 5575 (2001).
- [51] B. Huang, F. Yu, and R. N. Zare, Surface plasmon resonance imaging using a high numerical aperture microscope objective, *Anal. Chem.* **79**, 2979 (2007).
- [52] F. Bleckmann, Z. Cherpakova, S. Linden, and A. Alberti, Spectral imaging of topological edge states in plasmonic waveguide arrays, *Phys. Rev. B* **96**, 045417 (2017).
- [53] Z. L. Cao, S. L. Wong, S. Y. Wu, H. P. Ho, and H. C. Ong, High performing phase-based surface plasmon resonance sensing from metallic nanohole arrays, *Appl. Phys. Lett.* **104**, 171116 (2014).
- [54] S. L. Wong and H. C. Ong, Phase difference mapping of two-dimensional metallic nanohole arrays, *Appl. Phys. Lett.* **100**, 233102 (2012).
- [55] C. Liu and H. C. Ong, Realization of topological superlattices and the associated interface states in one-dimensional plasmonic crystals, *Phys. Rev. B* **106**, 045401 (2022).